Soft Matter

Accepted Manuscript

This is an *Accepted Manuscript*, which has been through the Royal Society of Chemistry peer review process and has been accepted for publication.

Accepted Manuscripts are published online shortly after acceptance, before technical editing, formatting and proof reading. Using this free service, authors can make their results available to the community, in citable form, before we publish the edited article. We will replace this *Accepted Manuscript* with the edited and formatted *Advance Article* as soon as it is available.

You can find more information about *Accepted Manuscripts* in the Information for Authors.

Please note that technical editing may introduce minor changes to the text and/or graphics, which may alter content. The journal's standard Terms & Conditions and the Ethical guidelines still apply. In no event shall the Royal Society of Chemistry be held responsible for any errors or omissions in this *Accepted Manuscript* or any consequences arising from the use of any information it contains.

ROYAL SOCIETY OF CHEMISTRY

www.rsc.org/softmatter

ARTICLE TYPE www. rsc.org/xxxxxx | XXXXXXXX

Relevance of saddle-splay elasticity in complex nematic geometries

Žiga Kos*[a] and Miha Ravnik[a]

Received Xth XXXXXXXXXX 20XX, Accepted Xth XXXXXXXXX 20XX
First published on the web Xth XXXXXXXXXX 200X
DOI: 10.1039/b000000x

We demonstrate the relevance of saddle-splay elasticity in nematic liquid crystalline fluids in the context of complex surface anchoring conditions and complex geometrical confinement. Specifically, nematic cells with patterns of surface anchoring and colloidal knots are shown as examples where saddle-splay free energy contribution can have a notable role which originates from nonhomogeneous surface anchoring and varying surface curvature. Patterned nematic cells are shown to exhibit various (meta)stable configurations of nematic field, with relative (meta)stability depending on the saddle-splay. We show that for high enough values of saddle-splay elastic constant K_{24} a previously unstable conformation can be stabilised, more generally indicating that saddle-splay can reverse or change the (meta)stability of various nematic structures and affecting their phase diagrams. Furthermore, we investigate saddle-splay elasticity in the geometry of highly curved boundaries – the colloidal particle knots in nematic – where local curvature of the particles induces complex spatial variations of the saddle-splay contributions. Finally, nematic order parameter tensor based saddle-splay invariant is shown, which allows for direct calculation of saddle-splay free energy from the Q-tensor, a possibility very relevant for multiple mesoscopic modelling approaches.

1 Introduction

Complex geometrical confinement of nematic liquid crystalline fluids by micro and nano-sized cavities, channels, topological objects and colloids is today an interesting direction for developing novel optical[1], photonic[2,3], rheological[4,5], topological[6,7] and microfluidic[8] materials. In such systems, the main variabilities are the geometry of the confining surfaces[6–8] and the alignment of the nematic imposed by the surfaces (i.e. surface anchoring)[8,9].

Complex surface conditions for nematic ordering can be achieved by patterning the surfaces with different surfactants, e.g. that impose partly perpendicular, partly inplane orientation of nematic molecules. In flat nematic cells, such approach can lead to sub-millisecond switching times of the nematic with electric field and is interesting for fast switching high-resolution displays[9]. Flat patterned cells may also exhibit a variety of nematic states with topological defects[10]. Patterned surface can be applied also to spheres[11–14] or tori[15], thus producing Janus colloids.

Geometric variability of nematic confinement is today impressively achieved by producing complex-shaped colloidal particles that take the shape of knots[6], nematic defect conditioned fibres[16], faceted particles[17–20] or handlebodies[7,21]. Contact surfaces between nematic fluid and the confining geometry can be also made micro-structured, with surface corrugations[22] and surface wrinkles[23,24]. The geometry and surface anchoring can be designed to give a working key-lock mechanism[25]. Another approach towards complex shaped objects is also by considering emulsions of nematic in host fluids, leading to complex shaped droplet fibres[3] and foams[26].

Nematic liquid crystalline fluids are soft materials with long range orientational order – characterised by nematic director $\mathbf{n}$ with $\mathbf{n} \leftrightarrow -\mathbf{n}$ symmetry – that effectively, responds elastically to external stimuli imposed by external fields or surfaces. Three basic elastic modes of nematic ordering are known to emerge – splay, twist and bend – which importantly, are further combined with elastic deformation modes know as saddle-splay and splay-bend. The elasticity effects are typically considered at the mesoscopic level, relying on the phenomenological expansion of the nematic free energy, as for example in Frank-Oseen or Landau-de Gennes formulation[27,28]. Notably, the Landau-de Gennes free energy minimisation is today used as one of the central approaches for modelling and predicting nematic liquid crystal fields because it can well account for the formation of topological defects[29–37]. It is actually well known that beside the standard splay, twist and bend elastic modes also saddle-splay elasticity is inherently incorporated in the Landau-de Gennes free energy (even with only one elastic constant), but typically little attention is given to its actual relevance when interpreting the results.

Saddle-splay elasticity has been of interest in experimental and theoretical studies. Periodic stripe deformation pattern was observed experimentally in a nematic confined between a

[a] *Faculty of Mathematics and Physics, University of Ljubljana, Slovenia. E-mail: ziga.kos@fmf.uni-lj.si*

homeotropic and a planar surface[38,39]. Numerical analysis has revealed the saddle-splay elasticity to be the driving force of creation of a stripe pattern. In similar geometries a set of point defects and strings was also observed, allowing for an estimation of saddle-splay elastic constant[40]. In nematic droplets, various configurations are observed and predicted, depending on the droplet size, anchoring of nematic molecules, and nematic elasticity. Saddle-splay was revealed to be a key element when calculating their stability criteria[41–43]. Experiments performed on biphenylic liquid crystals confined to cylindrical capillary with homeotropic anchoring[44,45] show at least four distinct configurations, whose stability is used to analytically determine the saddle-splay elastic constant. Numerical results confirm a great role of saddle-splay in capillary, specifically in the weak anchoring regime[46]. An experimental and theoretical study of lyotropic chromonic liquid crystals confined to capillary with planar degenerate boundary conditions reveals a chiral structure, which is a result of a large saddle-splay elastic modulus[47]. Similarly, saddle-splay was attributed to the chiral symmetry breaking in torus-shaped droplets[21,48]. Finally, the role of saddle-splay was investigated theoretically even for cholesteric liquid crystals under capillary confinement[49] and nematic shells[50].

Experimental[21,38,44,45] and numerical[51] works on saddle-splay free energy and its K_{24} elastic constant agree that K_{24} is indeed substantial and can be comparable in size to the standard Frank elastic constants (K_1, K_2, K_3), at least in a typical nematic representative 5CB material. Furthermore, recently unconventional elastic regimes have been reached in experiments, as for example in chromonic liquid crystals[52,53] or in twist-bend[54–56] and splay-bend[57] phase. Saddle-splay elastic constant in such materials is mostly unknown, however, it might be possible that such or similar materials could have also an unconventional saddle-splay elastic constant (as predicted in[47]) thus exhibiting some of the effects presented in this article.

If the nematic degree of order (scalar order parameter) is homogeneous, the saddle-splay elastic free energy can be rewritten into a form of a surface term, effectively renormalising the surface anchoring. Typically, this is the main reason why its contribution to the total free energy is (and can be) ignored. However, if the nematic geometry is complex and has complex boundaries, this surface integral may be of the same size as the splay, twist or bend elastic contributions and importantly, also spanning over regions which are defects (e.g. boojums or other). Even in view of homogeneous order parameter and defect-free configurations, there are two reasons how saddle-splay can be important: i) if the surface anchoring is small enough to allow for deviations from the preferred order at the boundary, as is the case in[38,39]. ii) If the anchoring is made degenerate, saddle-splay is made important by the local curvature of the boundary[21,47,48], or by patterning the surface with different anchoring regimes, as shown in this article. The idea of this paper is to show that in distinct complex confining geometries and surface anchoring configurations it is essential to consider also the saddle-splay elasticity, when exploring nematic fields. The examples of such geometries and surfaces include patterned cells[9] and complex shaped colloidal particles, like knots[6].

In this paper, we explore the saddle-splay free energy of nematic liquid crystalline fluids in complex geometries and in complex surface anchoring profiles, specifically demonstrating the important role of saddle-splay elasticity in patterned cells and in nematic colloidal knots. We consider saddle-splay elasticity in surface and volume free energy density formulations, taking advantage of both descriptions to demonstrate its role. Notably, we explore saddle-splay elasticity formulated by tensor order parameter free energy terms -rather than the standard director based formulation. We analyse the role of the elastic anisotropy in homeotropic-planar patterned cells for local hybrid aligned nematic and for boojum structures, finding that relative (meta)stability of the structures can be strongly affected by the actual value of the saddle-splay constant. We extend out analysis to colloidal knots, showing that regions of nematic boojum defects (which form at largest curvature regions of the particle knots) contribute via the saddle-splay as much as 37 % to the total elastic free energy if assuming single Landau elastic constant approximation ($2K_{24} = K_i = K$). Finally, we evaluate the mutual relation between tensor and director based formulation of the saddle-splay free energy.

2 Model and methods

The relevance of saddle-splay nematic deformation is explored within the general framework of the mesoscopic free energy, formulated in terms of nematic order parameter tensor $Q_{ij} = \frac{S}{2}(3n_in_j - \delta_{ij}) + \frac{P}{2}\left(e_i^{(1)}e_j^{(1)} - e_i^{(2)}e_j^{(2)}\right)$, which besides the scalar order parameter S and the director $\mathbf{n}$ includes also the biaxial ordering around second director $\mathbf{e}^{(1)}$ with biaxiality parameter P. The free energy is most commonly written in the Landau-de Gennes form:[27,58,59]

$$\begin{aligned} F = \int_V \Big\{ & \frac{A}{2}Q_{ij}Q_{ji} + \frac{B}{3}Q_{ij}Q_{jk}Q_{ki} + \frac{C}{4}(Q_{ij}Q_{ji})^2 \\ & + \frac{L_1}{2}\frac{\partial Q_{ij}}{\partial x_k}\frac{\partial Q_{ij}}{\partial x_k} + \frac{L_2}{2}\frac{\partial Q_{ij}}{\partial x_j}\frac{\partial Q_{ik}}{\partial x_k}\Big\}\mathrm{d}V \\ & + \int_{S^{\mathrm{uni}}} \frac{1}{2}W^{\mathrm{uni}}\left(Q_{ij} - Q_{ij}^0\right)^2 \mathrm{d}S \\ & + \int_{S^{\mathrm{deg}}} W^{\mathrm{deg}}\left[\left(\tilde{Q}_{ij} - \tilde{Q}_{ij}^{\perp}\right)^2 + \left(\tilde{Q}_{ij}^2 - \frac{9}{4}S_S^2\right)^2\right]\mathrm{d}S. \end{aligned} \tag{1}$$

First line of Eq. 1 describes the nematic bulk phase behaviour, where A, B, and C are material constants which determine the

bulk equilibrium nematic degree of order $S_{\rm eq}$. Second line corresponds to the effective nematic elastic free energy which we will denote also as $F_{\rm el}$. L_1 and L_2 are temperature independent (tensorial) elastic constants. Third line characterises the homeotropic anchoring surface free energy integrated over surface $S^{\rm uni}$. Q^0_{ij} is the surface-preferred order parameter tensor imposing homeotropic orientation of the director and bulk equilibrium value of the nematic degree of order and $W^{\rm uni}$ the surface anchoring strength. Fourth line gives planar degenerate surface free energy where $W^{\rm deg}$ is the anchoring strength $\tilde{Q}_{ij} = Q_{ij} + S_S\delta_{ij}/2$, $\tilde{Q}^{\perp}_{ij} = P_{ik}\tilde{Q}_{kl}P_{lj}$, $P_{ij} = \delta_{ij} - \nu_i\nu_j$, and ν_i is the surface normal. S_S is the surface-imposed degree of order which is set to $S_{\rm eq}$. Generally, the first two lines of Eq. 1 form the Landau-de Gennes free energy $F_{\rm LdG}$ and the last two lines form the surface anchoring free energy $F_{\rm a}$. The main advantage of the Q-tensor formulation of the free energy is that -besides the deformation of the director field- it also allows for modelling of the spatial variation of the nematic degree of order, thus better describing various experimental systems, in particular those with nematic defects. The director symmetry $\mathbf{n} \leftrightarrow -\mathbf{n}$ is also inherently incorporated in the tensor approach, making it a strong choice when calculating the nematic field profiles.

Nematic elastic free energy $F_{\rm el}$ formulated via the nematic order parameter tensor Q_{ij} can be rewritten (as well known from the literature[27,28]) into the form based on derivatives of the nematic director field $\mathbf{n}$, if assuming uniaxial Q_{ij} and homogeneous nematic degree of order. The result is the Frank-Oseen $F_{\rm F\text{-}O}$ and saddle-splay F_{24} free energy:[27,28]

$$F_{\rm F\text{-}O} = \int_V {\rm d}V \Big\{ \frac{1}{2}K_1(\nabla\cdot\mathbf{n})^2 + \frac{1}{2}K_2(\mathbf{n}\cdot\nabla\times\mathbf{n})^2 + \frac{1}{2}K_3(\mathbf{n}\times\nabla\times\mathbf{n})^2 \Big\}, \tag{2}$$

$$F_{24} = -\int_V {\rm d}V \Big\{ K_{24}\nabla\cdot[\mathbf{n}(\nabla\cdot\mathbf{n}) + \mathbf{n}\times\nabla\times\mathbf{n}] \Big\}, \tag{3}$$

where $F_{24} = \int_V {\rm d}V f^{\rm vol}_{24}$, K_1, K_2, K_3, and K_{24} are splay, twist, bend, and saddle-splay elastic constants, respectively. The elastic constants depend on temperature (or concentration, if considering lyotropic liquid crystals) and as such on the nematic degree of order S. Here, primarily for simplicity, we use only two (tensorial) elastic constants L_1 and L_2, which corresponds to $K_1 = K_3$. This identity can be broken by including the third (tensorial) elastic constant. The correspondence between the two used temperature independent (tensorial) elastic constants $L_i (i = 1,2)$ and Frank elastic constants K_i is as follows: $K_1 = K_3 = \frac{9S^2}{4}(2L_1 + L_2)$, $K_2 = \frac{9S^2}{2}L_1$, and $K_{24} = \frac{K_2}{2}$. For liquid crystal materials, the K_i set of elastic constants is typically measured. In the free energy formulation, splay-bend elastic terms can be also included[28,60–62]. This divergence term includes $\nabla^2\mathbf{n}$ elastic free energy density contribution, which is a higher order elastic term, and is typically not included in the Landau-de Gennes free energy formulation; therefore we do not consider it in this article.

Our numerical simulations are performed by minimising the total free energy by using finite difference relaxation algorithm on a cubic mesh[37]. The notable advantage of using this computationally simple method is that it is fast and also not very computer memory demanding, allowing us to simulate rather large simulation volumes, which qualitatively and even quantitatively compare well with experiments[6,16]. The minimisation is performed with *full* symmetric Q_{ij} tensor, and only after the equilibrium configuration is achieved, the director, nematic degree of order and other possible variables are calculated from the equilibrium Q_{ij} profile. In the simulations, the following values of the parameters are used: $A = -0.172\times 10^6\,{\rm Jm^{-3}}$, $B = -2.13\times 10^6\,{\rm Jm^{-3}}$, $C = 1.73\times 10^6\,{\rm Jm^{-3}}$, and mesh resolution $\Delta x = 10\,{\rm nm}$ which is sufficient to avoid defect pinning by the mesh. x_0, y_0, and z_0 are used to denote the size of the simulation box in x, y, and z directions. Mesh box equals $140\times 140\times 71$ points for patterned cells and $300\times 300\times 300$ points for colloidal knots. In the regime of a single elastic constant, we use $L_1 = 4\times 10^{-11}\,{\rm N}$ (and $L_2 = 0$). Chosen parameters roughly correspond to cyanobiphenilic liquid crystals[63,64]. In the elastically anisotropic regime, we use different ratios between elastic constants denoting the elastic anisotropy within the Frank-Oseen formulation as K_1/K_2. To preserve the lower estimate for the correlation length $\xi = 6.63\,{\rm nm}$ (important for numerical stability), the larger of the two elastic constants is increased when changing the elastic anisotropy at constant nematic degree of order, while keeping the relations $K_3 = K_1$ and $K_{24} = K_2/2$ preserved. The above material parameters correspond to dimensionless numerical parameters, set by $L_1(K_1 = K_2) = 1$ and $\xi = 1$, as follows: $A = -0.118$, $B = -2.341$, $C = 1.901$, $\Delta x = 1.5$. Preserving the lower estimate of the correlation length, the following transformation of dimensionless L_1 and L_2 is performed to characterise the K_1/K_2 ratio: $L_1 = K_2/K_1$, $L_2 = 2(1 - K_2/K_1)$ in the case of $K_1/K_2 \le 1$, and $L_1 = 1$, $L_2 = 2(K_1/K_2 - 1)$ in the case of $K_1/K_2 \ge 1$. Experimentally, similar elastic regimes could be achieved by the proper choice of the nematic material[52–57] or by tuning the temperature, and thus taking advantage of large deviations of elastic constants near nematic-isotropic[64,65] or nematic-smectic[66,67] phase transition.

2.1 Surface form of saddle-splay elasticity

Considering the Gauss theorem, the saddle-splay free energy can be rewritten into the surface integral form in the regime of homogeneous nematic degree of order[28]:

$$F_{24} = -\int_S {\rm d}S\boldsymbol{\nu}\cdot K_{24}\,[\mathbf{n}(\nabla\cdot\mathbf{n}) + \mathbf{n}\times\nabla\times\mathbf{n}] \tag{4}$$

where $\boldsymbol{\nu}$ is the surface normal. Notably, in such formulation the F_{24} can be considered as a surface free energy term, where

the integration is performed over the whole surface of a nematic. Defect cores are in principle excluded from the bulk integral in Eq. 2,3, which has to be considered also when defining the nematic surface in Eq. 4. Please note, that we write K_{24} under the integral, since in principle it depends on the inhomogeneous scalar order parameter ($K_{24} = K_{24}(S)$). In that way, it is possible to achieve a more accurate analysis of f_{24}^{surf} in boojum structures (Section 3.2), nevertheless still neglecting ∇S (and biaxiality) terms. In that case the surface integral in Eq. 4 can be performed over the whole outer surface of the nematic, regardless of the defect cores. However, due to inhomogeneity of S, Eq. 4 is only approximate as also spatial derivatives of S should have been included. For selected examples, the relative contributions are tested and reported in the paper. We mark f_{24}^{surf} as a saddle-splay surface free energy density ($F_{24} = \oint_S \mathrm{d}S f_{24}^{\mathrm{surf}}$), in contrast to *bulk* saddle-splay free energy density f_{24}^{bulk}. We provide the analysis of saddle-splay elasticity in complex nematic systems in view of volume (Eq. 3) and surface (Eq. 4) free energy density, which are calculated after the Q-tensor relaxation of the free energy (Eq. 1) has been performed.

If we consider a nematic cell, bounded by two horizontal planes and periodic boundary conditions in the lateral directions (as for example in Fig. 1a), the Eq. 4 can be further rewritten into

$$F_{24} = 2 \oint_S \mathrm{d}S K_{24} \left(\mathbf{n}_{\parallel} \cdot \nabla\right) n_{\perp}, \tag{5}$$

where $n_{\perp} = \boldsymbol{n} \cdot \boldsymbol{\nu}$ and $\boldsymbol{n}_{\parallel} = \boldsymbol{n} - n_{\perp}\boldsymbol{\nu}$. Considering Eq. 5, we see that f_{24}^{surf} is proportional to the derivatives of the normal component of the director along the in-plane director component. This indicates that the saddle-splay can become notable if the director varies within the plane of the surface; for example, if the anchoring is rather weak or if there is a border between different (strong) anchoring regimes (for example, boundary between strong homeotropic and strong planar anchoring).

Alternatively, Eq. 4 can be understood in terms of curvature of the boundary[48,68]. Under the assumption of strong (degenerate) planar surface anchoring, Eq. 4 can be rewritten into[48]:

$$F_{24} = \int_S \mathrm{d}S K_{24} \left(\kappa_1 n_1^2 + \kappa_2 n_2^2\right), \tag{6}$$

where κ_1 and κ_2 are the principal curvatures of the boundary and n_1 and n_2 are the components of the director along the directions of principal curvatures. This relation indicates that highly curved surfaces can also yield notable saddle-splay free energy contributions.

2.2 Tensor form of saddle-splay elasticity

Elastic anisotropy in liquid crystals is at the mesoscopic level generally described by introducing multiple invariants in the total free energy, each typically with a different elastic constants, which account for different elastic responses[69–71]. Saddle-splay is generally explored in the framework of nematic director, but today the majority of (numerical) calculations are performed with the nematic order parameter tensor. Therefore, specifically writing down the Q-tensor invariants that correspond to the saddle-splay seems a reasonable consideration, allowing for the direct evaluation of the saddle-splay elasticity. A possible formulation of the tensor-based saddle-splay volume free energy density f_{24}^{ten} can be written as:

$$f_{24}^{\mathrm{ten}} = L_{24} \left(\frac{\partial Q_{jk}}{\partial x_i} \frac{\partial Q_{ik}}{\partial x_j} - \frac{\partial Q_{ij}}{\partial x_j} \frac{\partial Q_{ik}}{\partial x_k} \right) \tag{7}$$

where L_{24} can be taken as the *tensorial* saddle-splay constant.

Eq. 7 is based on the well known and established relation between the director-based Frank-Oseen free energy and the Q-tensor-based Landau-de Gennes free energy, which can be related by assuming uniaxial form of the Q tensor and homogeneous profile of the nematic degree of order. Indeed, the Q tensor based saddle-splay free energy in Eq. 7 can be rewritten – by assuming uniaxial form of the Q-tensor – into:

$$f_{24}^{\mathrm{ten}} = -K_{24} \nabla \cdot [\mathbf{n}(\nabla \cdot \mathbf{n}) + \mathbf{n} \times \nabla \times \mathbf{n}] \tag{8}$$

$$- \frac{2K_{24}}{S} (\nabla \cdot \mathbf{n}) (\nabla S \cdot \mathbf{n}) + \frac{2K_{24}}{S} (\nabla S) [(\mathbf{n} \cdot \nabla) \mathbf{n}], \tag{9}$$

where $L_{24} = 4K_{24}/9S^2$. The fact that together both terms in Eq. 7 correspond to the saddle-splay contribution was already considered in the past[50,69,70]. In the case of two elastic constants L_1 and L_2, the relations between L_1, L_2, and K_{24} give $L_{24} = L_1$. In Supplementary Information we show that for $L_{24} = 4K_{24}/9S^2$, Eq. 7 can be mapped into Eq. 3 plus additional contributions arising from biaxiality and inhomogeneous S, as was also considered in the past[50,69,70].

We use tensor based and director based formulations of saddle-splay volume and surface density to demonstrate the importance of saddle-splay elasticity in complex geometrical confinement. Specifically, the two exemplary setups – as considered in Eq. 5 and Eq. 6 – provide us with an direct insight into the relevance of saddle-splay elastic free energy and are considered in the next sections. The importance of Eq. 5 can be demonstrated in nematic cells with patterned surface anchoring, where $n_{\perp}$ changes along the cell's boundary, whereas Eq. 6 clearly comes into account in nematics, confined by curved boundaries, as for example in the systems of knotted colloidal particles dispersed in nematic fluid.

3 Saddle-splay elasticity in nematic cells with patterned surface anchoring

In our first example we investigate saddle-splay elasticity in patterned cells, where anchoring at one cell surface (top) is

homeotropic whereas at the other surface (bottom) there is a circular patch of planar degenerate anchoring surrounded by homeotropic anchoring conditions (see Fig. 1a). In sections 3.1 and 3.2 we simulate two elasticity regimes $K_1 = K_2 = K_3$ and $K_1 = 2K_2 = K_3$ (with $W^{\mathrm{uni}} = W^{\mathrm{deg}} = 2 \times 10^{-3}\,\mathrm{J/m^2}$), respectively. In section 3.3 we investigate the nematic field for high values of K_2, which is not a typical elastic anisotropy regime of nematic liquid crystals but such elastic anisotropy is shown to allow for the formation of novel field configurations.

3.1 Local hybrid aligned nematic (HAN) configuration

Nematic profile with local hybrid aligned nematic director profile emerges in patterned cells in the regime of materials with roughly equal or similar elastic constants ($K_1 = 2K_2 = K_3$) (see Fig.1). The director field in such configuration shows a gradual transition from inplane orientation at the planar degenerate surface patch to the perpendicular at the homeotropic surfaces, as shown in Fig. 1b,c,d,e.

In one elastic constant regime ($K_1 = K_2 = K_3$), the in-plane director component $\mathbf{n}_\parallel$ is homogeneous throughout the bottom surface patch, with the actual direction of $\mathbf{n}_\parallel$ being arbitrary. The orientation along y axis was chosen for an easier analysis. The saddle-splay free energy density – calculated as surface free energy density f_{24}^{surf} or as volume free energy density f_{24}^{vol} – turns out to be substantial at the border line regions between the homeotropic and degenerate anchoring. The sign of saddle-splay free energy density locally depends on the structure of the nematic director, which effectively is determined by the direction of the hybrid alignment (i.e. the bend), as seen in Fig. 1e,f. Due to the symmetry of $\mathbf{n}_\parallel$, the locally negative and the positive values of f_{24}^{surf} and f_{24}^{vol} add up to zero (when performing the integration over surface or over bulk), giving no net saddle-splay free energy F_{24}.

In elastically anisotropic regime ($K_1 = 2K_2 = K_3$), the symmetry of the inplane director $\mathbf{n}_\parallel$ breaks and the net saddle-splay free energy F_{24} becomes non-zero, and actually notably contributing to the total elastic free energy (see Table 1). The regions contributing to this net value are close to the planar-homeotopic anchoring transition, where the director field gets additionally distorted compared to the elastically isotropic regime (Fig. 1b,c).

3.2 Boojum nematic configuration

The surface patterned cells allow – beside the local HAN configuration presented above – also for formation of the nematic profile with a surface boojum defect in the center of the planar patch, as shown in Fig. 2. Actually, in the considered patterned cell, we were able to generate three different boojum configurations via the initial conditions: a radial boojum, a hyperbolic boojum with winding number $+1$ (which we further call $+1$

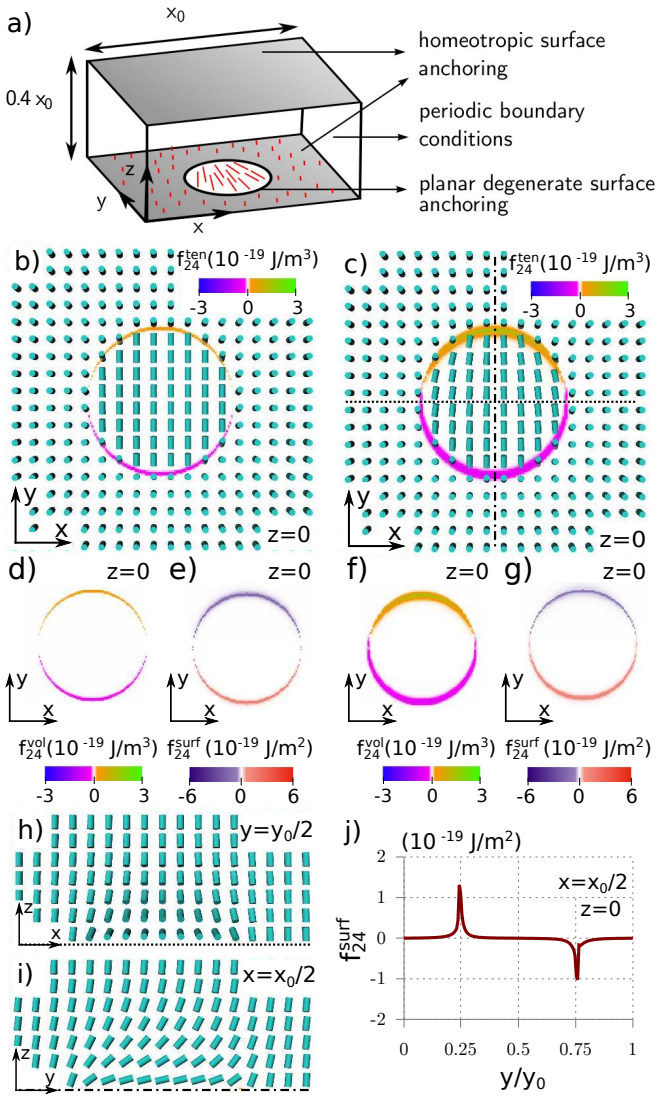

Fig. 1 Saddle-splay free energy in nematic cells with patterned surface anchoring. (a) Scheme of the nematic cell with patterned surface anchoring and periodic boundary conditions. (b) Director profile in a given cross-section and the corresponding tensor based saddle-splay free energy density f_{24}^{ten} at $z = 0$ for one elastic constant regime ($K_1 = K_2 = K_3$) and (c) elastically anisotropic regime ($K_1 = 2K_2 = K_3$). For comparison, director based volume f_{24}^{vol} and surface f_{24}^{surf} saddle-splay free energy densities are drawn for elastically isotropic (d,e) and anisotropic (f,g) regimes, respectively. (h,i) Director field in given cross-sections for elastically anisotropic regime. (j) Saddle-splay free energy surface density along the $z = 0$, $x = x_0/2$ axis. From (c) it is clearly seen that in the case of elastic anisotropy the symmetry of the saddle-splay density along the $y = y_0/2$ axis is broken (see especially the region close to the planar-homeotropic anchoring border). Patch diameter equals $x_0/2$.

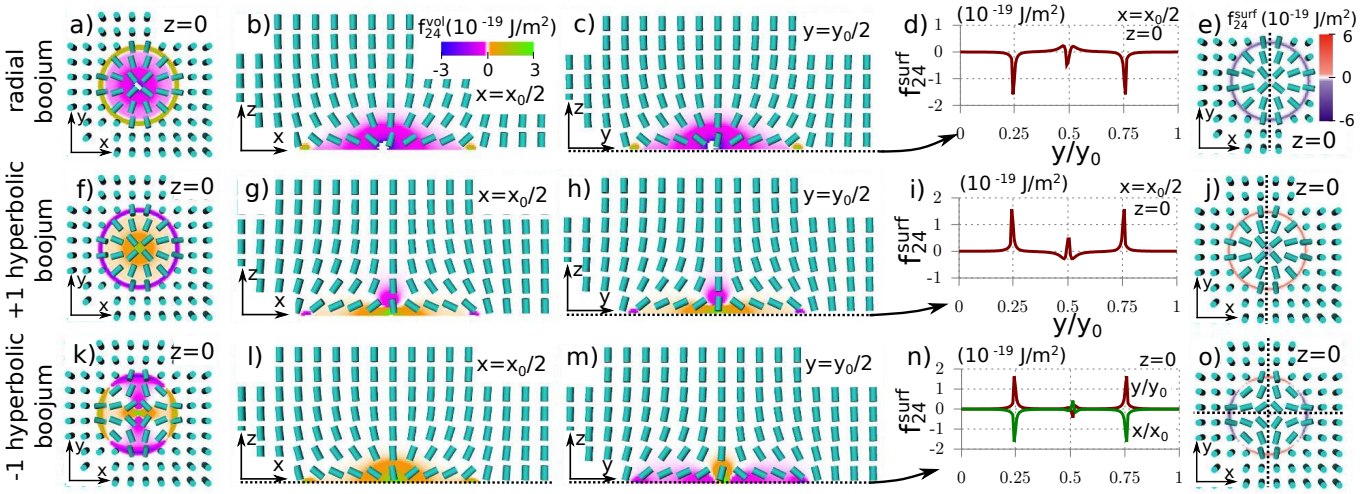

Fig. 2 Saddle-splay free energy in configurations with boojum defects. Director field profiles and the corresponding tensor based saddle-splay volume free energy density (1st, 2nd, and 3rd column) and director based saddle-splay surface free energy density (4th and 5th column) in the *xy* (first column), *xz* (second column), *yz* (4th and 5th column) cross-sections for (a-e) radial boojum, (f-j) +1 hyperbolic boojum, and (k-o) −1 hyperbolic boojum. Graphs in the 4th column represent the variation of saddle-splay surface free energy density along the *y* axis (and *x* in (n)) through the center of the bottom plane as marked by dotted lines.

hyperbolic boojum), and a hyperbolic boojum with winding number −1 (−1 hyperbolic boojum), all of them are presented in Fig. 2. Once formed, they turned out to be long-lived but were ultimately unstable and gradually deformed into a defect-free state (i.e. the local HAN configuration). Such behaviour is also reported to be observed experimentally[72]. These induced boojum states have for several 10% higher total free energy as the local HAN configuration.

The boojum configurations allow us to evaluate the saddle-splay free energy in comparison to other free energy contributions (Table 1), and to analyse the spatial profiles of the saddle-splay contributions to the free energy, especially in the red view of topological defects. The saddle-splay free energy density profiles are distinctly different, as compared to the HAN configuration where locally positive and negative contributions mostly cancelled each other out in the total saddle-splay free energy F_{24}. In the boojum configurations, the saddle-splay volume free energy density f_{24}^{vol} is substantial close to the degenerate surface, but moreover in the region of the central boojum defect (Fig. 2b,c,g,h,l,m). For the radial boojum in Fig. 2a-e), f_{24}^{vol} is mostly positive. For the +1 hyperbolic boojum in Fig. 2f-j, f_{24}^{vol} has regions of both negative an positive values with leadingly positive regions. For the −1 hyperbolic boojum structure (Fig. 2k-o), f_{24}^{vol} shows a complex spatial profile where regions of positive and negative f_{24}^{vol} mostly cancel each other out and F_{24} thus contributes only little to the total elastic free energy (Table 1). The profile of the saddle-splay volume density in boojum configurations explains the substantial contributions of saddle-splay elasticity to the total elastic free energy for radial and +1 hyperbolic configurations and much smaller saddle-splay free energy for a −1 hyperbolic boojum. Since the main contributions arise from regions close to boojum defect cores, the knowledge of boojums could potentially suffice to deduce the amount (or the sign) of saddle-splay free energy in general systems with surface boojum defects.

Considering the saddle-splay as the surface term f_{24}^{surf}, it is primarily conditioned by the contributions from the the planar-homeotropic anchoring boundary. At this boundary region, f_{24}^{surf} is negative for the radial boojum (Fig. 2d,e), it is positive for the +1 hyperbolic boojum (Fig. 2i,j), and the sign varies for the −1 hyperbolic boojum (Fig. 2n,o). The f_{24}^{surf} shows variations close to the defect cores; however, they are suppressed by the low values of the nematic degree of order. However, although contributions of f_{24}^{surf} arise from the director distortions at the planar-homeotropic anchoring border, the total value of F_{24} is still conditioned by the possible occurrence of a boojum at the center of a planar degenerate surface. In the absence of a boojum (i.e. HAN configuration) or in the case of a −1 hyperbolic boojum, f_{24}^{surf} at the planar-homeotropic anchoring border mostly cancel each other out. In the case of a radial or +1 hyperbolic boojum, the sign of F_{24}^{surf} stays the same throughout the planar-homeotropic anchoring transition and thus f_{24}^{surf} contributes a substantial amount to the total elastic free energy (Table 1).

Changing the elastic constants to $K_1 = 2K_2 = K_3$ has little effect on the nematic field in boojum states. The free energy of boojum states remains few 10 % higher than for HAN

configuration. In radial and +1 hyperbolic configuration, the change of the elastic constants mostly increased the weight of splay and bend deformations thus reducing the saddle-splay contribution to the elastic energy, while in −1 hyperbolic state the applied change in elastic anisotropy changed the balance towards positive value of F_{24} (Table 1). Free energy contributions for higher elastic anisotropy are given in Table 1. We see that for HAN configuration an anisotropic elastic condition was necessary to induce a nonzero saddle-splay elasticity. For radial and +1 hyperbolic boojum configurations F_{24} contributed a larger amount to the total elastic free energy also in the one elastic constant regime. The change of elastic constants affected the F_{24}/F_{el} ratio, however the saddle-splay free energy remains substantial. Compared to other boojum states, F_{24} for a −1 hyperbolic boojum is relatively small, which does not change much in different elastic regime.

Table 1 Saddle-splay free energy F_{24} contributions to the total elastic free energy F_{el} in patterned cells. F_{24} is calculated as the bulk integral (Eq. 3)

	F_{24}/F_{el} for $K_1 = K_2 = K_3$	F_{24}/F_{el} for $K_1 = 2K_2 = K_3$
HAN configuration	0	4.9
radial boojum	−0.34	−0.15
+1hyperbolic boojum	0.36	0.27
−1 hyperbolic boojum	−0.012	0.038

We use the calculated boojum and HAN configurations to test the relevance of Eq. 4 (the surface director formulated saddle-splay free energy density). For the HAN configuration, we can calculate Eq. 4 at homogeneous nematic degree of order S_{eq} without the numerical difficulties due to singularities in the director field. The results agree with F_{24}, calculated from Eq. 3 up to a negligible numerical relative error of 4×10^{-6}. However, if spatially dependent nematic degree of order S is taken as calculated from the order parameter tensor, the Eq. 4 can deviate from Eq. 3 for up to 24 %[73]. This discrepancy is rather notable not only in the boojum configurations, but actually emerges also in the elastically anisotropic hybrid aligned configuration (Section 3.1). Therefore, more generally, if nematic degree of order S varies throughout the sample, Eq. 4 can be taken (as expected) only as an estimate for calculating the the saddle-splay free energy contribution. For exact computation of the saddle-splay free energy, the bulk formulation of the saddle-splay free energy needs to be evaluated (Eq. 3).

3.3 Stabilisation of radial boojum via saddle-splay

Strongly negative values of the saddle-splay free energy of the radial boojum configuration suggest that for high saddle-splay coupling such state could potentially become not only long-lived but metastable or even stable. Indeed, we demonstrate that this can be achieved by increasing the elastic anisotropy ratio K_2/K_1 where $K_{24} = K_2/2$ and $K_1 = K_3$, effectively increasing the saddle-splay elastic constant K_{24}. The free energy of the radial boojum configuration falls below the free energy of the HAN configuration at $K_2/K_1 \sim 2$ and becomes the equilibrium configuration, which is shown in Fig 3. When increasing the K_2/K_1 ratio, the free energy configurations show a decrease in the difference between Frank-Oseen free energies, but a rather constant large difference between the saddle-splay free energies of the two states, which causes the stabilisation that can be attributed to the saddle-splay. More broadly, this indicates that the actual values of the saddle-splay constant in different systems can be a major factor in determining stability, metastability or non-stability of different structures.

Models which include only Frank-Oseen and not also the saddle-splay free energy could not properly predict the stability of a radial boojum at $K_2/K_1 \sim 2$. Although our simulation includes saddle-splay elasticity and does not correspond exactly to Frank-Oseen free energy minimisation, Fig. 3 indicates that Frank-Oseen free energy of a radial boojum should fall below the Frank-Oseen free energy of the HAN configuration at much higher elastic anisotropy than $K_2/K_1 \sim 2$ and therefore, such behaviour could not be fully explained in terms of solely Frank-Oseen elasticity.

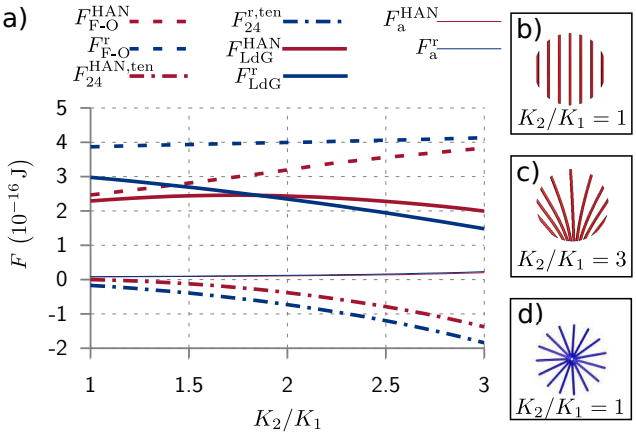

Fig. 3 Stabilisation of boojum configuration via saddle-splay (a) Free energy contributions for the HAN configuration (superscript HAN, in red) and the radial boojum configuration (superscript r, in blue) as dependent on the elastic anisotropy K_2/K_1 where $K_{24} = K_2/2$. At higher values of K_2/K_1, the free energy of the radial boojum falls below the value of the HAN configuration. Note that the relative amount of the saddle-splay energy increases with the elastic anisotropy. F_{LdG} is plotted as a difference to the Landau-de Gennes free energy of an undistorted homogeneous nematic of the same volume. The snapshots of the director field at the bottom degenerate planar patch are presented for (b,c) the HAN configuration and (d) radial boojum configuration. Surface anchoring was set to $W^{\mathrm{uni}} = 0.01\,\mathrm{J/m^2}$ and $W^{\mathrm{deg}} = 0.01\,\mathrm{J/m^2}$.

4 Saddle-splay elasticity in planar degenerate colloidal knots

The relevance of curved boundaries in the saddle-splay free energy are demonstrated for the case of colloidal knots with planar degenerate boundary conditions. Experimentally and with numerical modelling they were explored in Ref.[6]. We simulate the trefoil $(3,2)$ and pentafoil $(5,3)$ torus knots as tubes of the following parametric curves:

$$\begin{aligned}\mathbf{r}_{(3,2)} = (&2.1R(\cos\phi - 2.25\cos 2\phi),\\ &2.1R(\sin\phi + 2.25\sin 2\phi),\\ &6R\sin 3\phi),\end{aligned} \tag{10}$$

$$\begin{aligned}\mathbf{r}_{(5,3)} = (&2.75R(\cos 3\phi - 3\cos 2\phi),\\ &2.75R(\sin 3\phi + 3\sin 2\phi),\\ &6R\sin 5\phi),\end{aligned} \tag{11}$$

similar to[6], where $\phi \in [0, 2\pi)$ and $R = 10\Delta x$ is the knot size parameter. Knots are of the width $d_0 = 12.5\Delta x$. The director field at the boundaries of the simulation box is assumed to be homogeneous along the z direction. One elastic constant approximation and anchoring strength of $W^{\mathrm{deg}} = 4\times10^{-3}\,\mathrm{J/m^2}$ are used.

The trefoil knot generates 12 boojums as shown in Fig. 4b,c,d,e) in red color, which emerge at the regions of highest local curvature, i.e. local saddle points and local peaks. These boojums emerge as $+$ and $-$ pairs, satisfying the topological constraints of the knot[6]. Analogously as the trefoil knot, the pentafoil knot generates 20 boojums, again at highest-local curvature locations, as seen from Fig. 4.

The saddle-splay free energy density f_{24}^{surf} shows for both the trefoil and pentafoil knots a distinctive pattern, which can be partially explained by Eq. 6. Possible values of f_{24}^{surf} depend on the local curvature of the particle knot and since the major part of the knot's surface has positive curvature the f_{24}^{surf} is mostly positive. In the vicinity of the hyperbolic boojums (bottom one in Fig. 4b,c), $f_{24}^{\mathrm{surf}} > 0$ if the director bends along the direction of positive principal curvature, and $f_{24}^{\mathrm{surf}} < 0$ if the director bends along the direction of the negative principal curvature. However, beside Eq. 6 there are additional surface contributions to the saddle-splay free energy, which arise due to finite anchoring strength. In the vicinity of $+1$ hyperbolic boojums, the normal component of the director increases along the surface in a manner that is similar to the planar-homeotropic alignment border in the case of a radial boojum in a patterned cell (Fig. 2b,c). This variation of the director field along the surface explains negative areas of f_{24}^{surf} around $+1$ hyperbolic boojums, as seen in Fig. 4a. Elsewhere along the surface, the variations from the surface-preferred director orientation are (i) not strong enough or (ii) in agreement with saddle-splay contributions arising from local curvature and cause no specific pattern to occur.

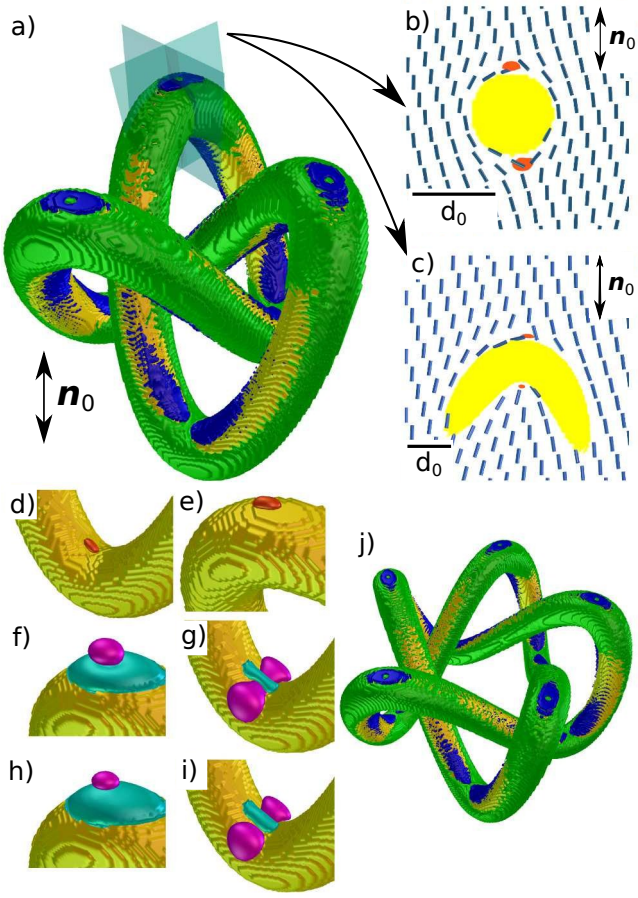

Fig. 4 Saddle-splay free energy in complex curved geometry of knotted colloidal particles. (a) Saddle-splay surface free energy density plotted at the surface of the trefoil colloidal knot. Surface of the particle is plotted in yellow, green color corresponds to isosourface of positive saddle-splay surface free energy density $f_{24}^{\mathrm{surf}} = 10^{-21}\,\mathrm{J/m^2}$, and blue to isosurface of negative saddle-splay surface free energy density $f_{24}^{\mathrm{surf}} = -10^{-21}\,\mathrm{J/m^2}$. Director far-field is marked by $\mathbf{n}_0$. (b,c) Two detailed views of the director field in given cross-sections with indicated boojums as isosurfaces of $S = 0.4$ shown in red. (d,e) Boojum defects at the particles knots drawn in red as isosurfaces of $S = 0.4$. (f,g) Volume density of a director based saddle-splay free energy F_{24} compared to the (h,i) tensor based F_{24}^{ten} shows little difference, supporting the fact that primarily the director deformations are responsible for the tensor based free energy density profiles. The isosurfaces are drawn at $5\times10^{-21}\,\mathrm{J/m^3}$ in light blue and at $-0.6\times10^{-21}\,\mathrm{J/m^3}$ purple. (j) Saddle-splay surface free energy density f_{24}^{surf} of the pentafoil knot. Surface of the particle is plotted in yellow, green color corresponds to isosourface of $f_{24}^{\mathrm{surf}} = 10^{-21}\,\mathrm{J/m^2}$, and blue isosurface of $f_{24}^{\mathrm{surf}} = -10^{-21}\,\mathrm{J/m^2}$.

Figures 4f,g show saddle-splay volume free energy density

f_{24}^{vol}. Close to the $+1$ hyperbolic boojum, f_{24}^{vol} is mostly positive. This shows similarity to f_{24}^{vol} in patterned cells, only that in the case of knots the area with negative f_{24}^{vol} is suppressed near $+1$ hyperbolic boojums. There is even greater similarity in the case of -1 hyperbolic boojum. Both Fig. 4f and Fig. 2l,m show a region of $f_{24}^{\mathrm{vol}} > 0$, surrounded by two regions where $f_{24}^{\mathrm{vol}} < 0$.

More generally, the calculated results agree with anticipating positive saddle-splay free energy because of primarily positive curvature of the investigated colloidal knots. The analysis of the saddle-splay elasticity in combination with flat and curved geometry now also suggests that boojums indicate the structure of saddle-splay free energy density, where in particular $+1$ hyperbolic boojums give positive contributions to the saddle-splay free energy and radial boojums give negative contributions to F_{24}. Calculating the total saddle-splay free energy of the knotted colloids F_{24}, it is in fact positive and represents a substantial part of the total elastic free energy F_{el} for a trefoil and a pentafoil knot as shown in Table 2.

Table 2 Saddle-splay contribution to the total elastic free energy in colloidal knots with planar degenerate anchoring

	trefoil particle knot $(3,2)$	pentafoil particle knot $(5,3)$
F_{24}/F_{el}	0.37	0.34

5 Comparison between tensor and director formulated saddle-splay free energy

Exact comparison between tensorial and director-based consideration of saddle-splay is important when exact values of free energies are needed, e.g. when predicting stability or structural transitions between different nematic (meta)stable structures or profiles. Fig. 1 and Fig. 4 reveal clearly similar profiles of the director based and tensor based saddle-splay free energy density, however, selected differences between both approaches can be observed. Here, we provide a further more quantitative analysis of the individual contributions to the difference between director and tensor based approaches. We show the use of Q-tensor saddle-splay free energy F_{24}^{ten} for the example of a radial boojum structure in a patterned cell within one elastic constant regime (Fig. 2a-e, Section 3.2). The results are presented in Table 3, where ∇S and biaxial contributions, total discrepancy between F_{24} and F_{24}^{ten}, and the error resulting from finite mesh resolution are calculated at two mesh resolutions. Note that the tensorial saddle-splay free energy Eq. 7 is not explicitly incorporated as a new free energy contribution to the total free energy, but is actually already an inseparable part of the standard one elastic constant Landau-de Gennes free energy F_{LdG}. Single elastic invariant $\frac{\partial Q_{ij}}{\partial x_k}\frac{\partial Q_{ij}}{\partial x_k}$ from F_{LdG} incorporates not only splay, bend, and twist deformation modes but also saddle-splay.

There are three main differences between the tensor based saddle-splay free energy F_{24}^{ten} and director based saddle-splay free energy F_{24}: (i) possible local biaxiality of Q_{ij} (in particular in the defect cores), (ii) ∇S terms (relevant in the defect regions), and (iii) numerical error due to finite mesh resolution (we use $\Delta x/\xi = 1.5$). The biaxial contribution to F_{24}^{ten} is evaluated by taking only the uniaxial part of the calculated Q_{ij} and re-evaluating Eq. 7. The ∇S contributions are calculated explicitly from the diagonalisation of the Q-tensor profile. The rest of the discrepancy between F_{24}^{ten} and F_{24} is attributed to finite resolution, which we quantify by modelling exactly the same structure with two resolutions ($\Delta x = 10\,\mathrm{nm}$ and $\Delta x/2 = 5\,\mathrm{nm}$). Indeed, the finite difference algorithm with rather large mesh resolution ($\Delta x/\xi \sim 1$) suffers from rather low precision at the determination of the exact value of the total free energy. Especially the explicit calculation of saddle-splay free energy, as done in this article at sharp surface anchoring boundaries, gives a limited precision of $\sim 20\%$ due to finite resolution. Finer resolution or, especially in the case of curved interfaces, finite elements methods could be used to investigate saddle-splay free energy density with higher precision. Table 3 shows that director deformations are still the most significant part of the f_{24}^{ten}, which is in agreement with the comparison between director based and tensor based free energy density profiles in Fig. 4.

Table 3 Relative contributions in Q-tensor saddle-splay free energy F_{24}^{ten} as compared to director based F_{24}. They are calculated at the resolution Δx and at $\Delta x/2$ keeping the same physical sample size. Finite resolution error in the last column is calculated by explicitly subtracting ∇S and biaxial contributions from F_{24}^{ten} and reevaluating $\frac{F_{24}-F_{24}^{\mathrm{ten}}}{F_{24}}$.

Mesh resolution	∇S terms (Eq. 9)	biaxial contribution	$\frac{F_{24}-F_{24}^{\mathrm{ten}}}{F_{24}}$	finite resolution error
Δx	$-0.11\,F_{24}^{\mathrm{dir}}$	$-0.07\,F_{24}^{\mathrm{dir}}$	0.39	0.21
$\Delta x/2$	$-0.12\,F_{24}^{\mathrm{dir}}$	$-0.08\,F_{24}^{\mathrm{dir}}$	0.33	0.13

To generalise, f_{24}^{ten} represents an easy-to-implement measure of saddle-splay elasticity in terms of Q-tensor. Due to the nature of Q-tensor formalism, discrepancy between saddle-splay free energy, calculated in director or tensorial approach, may occur and is actually expected to occur –in particular in systems with large variations of nematic degree of order and possibly even biaxiality, which is often the case in complex geometrical confinements.

6 Conclusions

We have explored the relevance of saddle-splay elasticity in complex nematic geometries, with particular focus on nematic systems with inhomogeneous (patterned) surface anchoring and with complex surface curvatures. Saddle-splay elasticity was analysed in the view of volume and surface density, where the latter can be considered only as an approximation if nematic degree of order is inhomogeneous. Specifically, we investigated the saddle-splay elasticity in patterned cells and around colloidal knots.

In the first example of patterned cells, the large saddle-splay contributions F_{24} to the total free energy emerge from the border region between the planar and homeotropic anchoring patches, as seen from both surface and volume saddle-splay free energy formulations. To vary the magnitude of the saddle-splay free energy F_{24}, elastic anisotropy is used, which helps in achieving a larger stability window of the simulations. Negative values of F_{24} of a radial structure on the surface patch make it possible to reduce its free energy below the free energy of the hybrid aligned configuration if K_2 and K_{24} are large enough, showing that saddle-splay elasticity can condition the ground state of nematic in geometries with complex surface.

In the second example of colloidal knots, the largest saddle-splay contributions to the total free energy are shown to emerge from the highest local curvature regions, which actually also coincide with the locations of surface boojum defects. Generally, in the colloidal knots, F_{24} is large due to surface variations of normal director component and due to high curvature of colloidal knots. The spatial profiles of the saddle-splay volume free energy are calculated, and shown to distinctly depend on the boojum-type, i.e. its topological structure. Indeed, boojum structures that appear at the trefoil $(3,2)$ and pentafoil $(5,3)$ colloidal knots have similar spatial profile of the saddle-splay free energy density f_{24}^{vol} as in patterned cells.

We explored saddle-splay formulated as a Q-tensor (not director) term $\frac{\partial Q_{jk}}{\partial x_i}\frac{\partial Q_{ik}}{\partial x_j} - \frac{\partial Q_{ij}}{\partial x_j}\frac{\partial Q_{ik}}{\partial x_k}$. The contributions to the tensor-based saddle-splay free energy are shown to be in the range of several 10% with the magnitudes strongly depending on the actual considered nematic geometry, in particular on the presence of topological defects. Such tensor based saddle-splay free energy is significantly influenced by ∇S and biaxial terms, but represents a directly implementable way to calculate saddle-splay contribution to the free energy in a given nematic field.

More generally, in the explored structures, the saddle-splay free energy is found to contribute substantially to the total free energy, thus affecting the stability or metastabilty of the structures. Nematic profiles in complex geometries typically form a range of (meta)stable states, with their mutual stability or metastability conditioned by the exact value of the total free energy minimum. Therefore, when considering phase-diagrams or stability in complex nematic structures the relevance of saddle-splay – i.e. the actual value of saddle-splay elastic constant K_{24} – has to be considered. Finally, the presented work is a contribution towards understanding the stability and formation of complex structures in general nematic complex fluids, including liquid crystal and active nematics.

Acknowledgements

The authors acknowledge stimulating discussions and joint work on topics related to this work with S. Žumer, L. Cattaneo, T. Rasing, I. Muševič, and I. I. Smalyukh. Financial support from SLO ARRS program P1-0099, project Z1-5441, and EU MC program FREEFLUID is acknowledged.

References

1 F. Castles, S. M. Morris, J. M. C. Hung, M. M. Qasim, A. D. Wright, S. Nosheen, S. S. Choi, B. I. Outram, S. J. Elston, C. Burgess, L. Hill, T. D. Wilkinson and H. J. Coles, *Nat. Mater.*, 2014, **13**, 817.
2 J. Beeckman, K. Neyts and P. V. M. Vanbrabant, *Opt. Eng.*, 2011, **50**, 081202.
3 K. Peddireddy, V. S. R. Jampani, S. Thutupalli, S. Herminghaus, C. Bahr and I. Muševič, *Opt. Express*, 2013, **21**, 30233.
4 T. Sanchez, D. T. N. Chen, S. J. DeCamp, M. Heymann and Z. Dogic, *Nature*, 2012, **491**, 431.
5 K. Drescher, J. Dunkel, L. H. Cisneros, S. Ganguly and R. E. Goldstein, *Proc. Natl. Acad. Sci.*, 2011, **108**, 10940.
6 A. Martinez, M. Ravnik, B. Lucero, R. Visvanathan, S. Žumer and I. I. Smalyukh, *Nat. Mater.*, 2014, **13**, 258.
7 B. Senyuk, Q. Liu, S. He, R. D. Kamien, R. B. Kusner, T. C. Lubensky and I. I. Smalyukh, *Nature*, 2013, **493**, 200.
8 A. Sengupta, S. Herminghaus and C. Bahr, *Liquid Crystals Reviews*, 2014, **2**, 73.
9 J. Zhang, M. I. Boamfa, A. E. Rowan and T. Rasing, *Adv. Mater.*, 2010, **22**, 961.
10 P. Guillamat, F. Sagués and J. Ignés-Mullol, *Phys. Rev. E*, 2014, **89**, 052510.
11 M. Conradi, M. Ravnik, M. Bele, M. Zorko, S. Žumer and I. Muševič, *Soft Matter*, 2009, **5**, 3905.
12 M. Melle, S. Schlotthauer, M. G. Mazza, S. H. L. Klapp and M. Schoen, *J. Chem. Phys.*, 2012, **136**, 194703.
13 Y. Iwashita and Y. Kimura, *Soft Matter*, 2013, **9**, 10694.
14 S. Čopar, M. Ravnik and S. Žumer, *Materials*, 2014, **7**, 4272.
15 M. Cavallaro Jr, M. A. Gharbi, D. A. Beller, S. Čopar, Z. Shi, R. D. Kamien, S. Yang, T. Baumgart and K. J. Stebe, *Soft Matter*, 2013, **9**, 9099.
16 M. Nikkhou, M. Škarabot, S. Čopar, M. Ravnik, S. Žumer and I. Muševič, *Nature Phys.*, 2015, **11**, 183.
17 F. R. Hung and S. Bale, *Molecular Simulation*, 2009, **35**, 822.
18 J. S. Evans, C. N. Beier and I. I. Smalyukh, *J. Appl. Phys.*, 2011, **110**, 033535.
19 D. Engström, R. P. Trivedi, M. Persson, M. Goksör, K. A. Bertness and I. I. Smalyukh, *Soft Matter*, 2011, **7**, 6304.
20 D. A. Beller, M. A. Gharbi and I. B. Liu, *Soft Matter*, 2015, **11**, 1078.
21 E. Pairam, J. Vallamkondu, V. Koning, B. C. van Zuiden, P. W. Ellis, M. A. Bates, V. Vitelli and A. Fernandez-Nieves, *Proc. Natl. Acad. Sci.*, 2013, **110**, 9295.

22 N. M. Silvestre, Z. Eskandari, P. Patrício, J. M. Romero-Enrique and M. M. T. da Gama, *Phys. Rev. E*, 2012, **86**, 011703.
23 A. C. Trindade, J. P. Canejo, L. F. V. Pinto, P. Patríco, P. Brogueira, P. I. C. Teixeira and M. H. Godinho, *Macromolecules*, 2011, **44**, 2220.
24 T. Ohzono, T. Yamamoto and J. Fukuda, *Nat. Commun.*, 2014, **5**, 3735.
25 N. M. Silvestre, Q. Liu, B. Senyuk, I. I. Smalyukh and M. Tasinkevych, *Phys. Rev. Lett.*, 2014, **112**, 225501.
26 S. Shi and H. Yokoyama, *Langmuir*, 2015, **31**, 4429.
27 P. G. de Gennes and J. Prost, *The Physics of Liquid Crystals*, Oxford University Press, New York, 1993.
28 M. Kleman and O. D. Lavrentovich, *Soft Matter Physics: An Introduction*, Springer Verlag Inc., New York, 2003.
29 G. Alexander and J. Yeomans, *Phys. Rev. E*, 2006, **74**, 061706.
30 M. A. Lohr, M. Cavallaro, D. A. Beller, K. J. Stebe, R. D. Kamien, P. J. Collings and A. G. Yodh, *Soft Matter*, 2014, **10**, 3477.
31 O. Henrich, K. Stratford, M. E. Cates and D. Marenduzzo, *Phys. Rev. Lett.*, 2011, **106**, 107801.
32 J. Fukuda, *Phys. Rev. E*, 2010, **82**, 061702.
33 S. M. Hashemi and M. R. Ejtehadi, *Phys. Rev. E*, 2015, **91**, 012503.
34 K. Tojo, A. Furukawa, T. Araki and A. Onuki, *Eur. Phys. J. E*, 2009, **30**, 55.
35 F. R. Hung, O. Guzmán, B. T. Gettelfinger, N. L. Abbott and J. J. de Pablo, *Phys. Rev. E*, 2006, **74**, 011711.
36 M. Tasinkevych, N. Silvestre, P. Patrício and M. T. da Gama, *Eur. Phys. J. E*, 2002, **9**, 341.
37 M. Ravnik and S. Žumer, *Liq. Cryst.*, 2009, **36**, 1201.
38 A. Sparavigna, O. Lavrentovich and A. Strigazzi, *Phys. Rev. E*, 1994, **49**, 1344.
39 A. Sparavigna, L. Komitov, O. D. Lavrentovich and A. Strigazzi, *J. Phys. II France*, 1992, **2**, 1881.
40 O. D. Lavrentovich, *Phys. Scr.*, 1991, **39**, 394.
41 S. Žumer and S. Kralj, *Liq. Cryst.*, 1992, **12**, 613.
42 D. S. Miller and N. L. Abbott, *Soft Matter*, 2013, **9**, 374.
43 J. Gupta, S. Sivakumar, F. Caruso and N. Abbott, *Angew. Chem. Int. Ed.*, 2009, **48**, 1652.
44 D. Allender, G. Crawford and J. Doane, *Phys. Rev. Lett.*, 1991, **67**, 1442.
45 R. Polak, G. Crawford, B. Kostival, J. Doane and S. Žumer, *Phys. Rev. E*, 1994, **49**, R978.
46 S. Kralj and S. Žumer, *Phys. Rev. E*, 1995, **51**, 366.
47 Z. S. Davidson, L. Kang, J. Jeong, T. Still, P. J. Collings, T. C. Lubensky and A. G. Yodh, *Phys. Rev. E*, 2015, **91**, 050501.
48 V. Koning, B. C. van Zuiden, R. D. Kamien and V. Vitelli, *Soft Matter*, 2014, **10**, 4192.
49 A. Kilian and A. Sonnet, *Phys. Rev. E*, 1995, **52**, 2702.
50 S. Kralj, R. Rosso and E. G. Virga, *Soft Matter*, 2011, **7**, 670.
51 A. A. Joshi, J. K. Whitmer, O. Guzmán, N. L. Abbott and J. J. de Pablo, *Soft Matter*, 2014, **10**, 882.
52 L. Tortora and O. D. Lavrentovich, *Proc. Natl. Acad. Sci.*, 2011, **108**, 5163.
53 J. Jeong, Z. S. Davidson, P. J. Collings, T. C. Lubensky and A. G. Yodh, *Proc. Natl. Acad. Sci.*, 2014, **111**, 1742.
54 V. Borshch, Y.-K. Kim, J. Xiang, M. Gao, A. Jákli, V. P. Panov, J. K. Vij, C. T. Imrie, M. G. Tamba, G. H. Mehl and O. D. Lavrentovich, *Nat. Commun.*, 2013, **4**, 2635.
55 S. M. Shamid, S. Dhakal and J. V. Selinger, *Phys. Rev. E*, 2013, **87**, 052503.
56 D. Chen, M. Nakata, R. Shao, M. R. Tuchband, M. Shuai, U. Baumeister, W. Weissflog, D. M. Walba, M. A. Glaser, J. E. Maclennan and N. A. Clark, *Phys. Rev. E*, 2014, **89**, 022506.
57 P. Sathyanarayana, M. Mathew, Q. Li, V. S. S. Sastry, B. Kundu, K. V. Le, H. Takezoe and S. Dhara, *Phys. Rev. E*, 2010, **81**, 010702.
58 M. Nobili and G. Durand, *Phys. Rev. A*, 1992, **46**, R6174.
59 J.-B. Fournier and P. Galatola, *Europhys. Lett.*, 2005, **72**, 403.
60 V. M. Pergamenshchik, *Phys. Rev. E*, 1993, **48**, 1254.
61 S. Ponti, *Physics Letters A*, 1995, **200**, 165.
62 G. Barbero and G. Durand, *Phys. Rev. E*, 1993, **48**, 1942.
63 M. Cui and J. R. Kelly, *Mol. Cryst. Liq. Crys. A*, 1999, **331**, 49.
64 N. V. Madhusudana and R. Pratibha, *Mol. Cryst. Liq. Cryst.*, 1982, **89**, 249.
65 H. Schad, *J. Chem. Phys.*, 1981, **75**, 880.
66 J. Huang and J. T. Ho, *Phys. Rev. Lett.*, 1987, **58**, 2239.
67 J. Huang and J. T. Ho, *Phys. Rev. A*, 1990, **42**, 2449.
68 R. Kamien, *Rev. Mod. Phys.*, 2002, **74**, 953.
69 K. Schiele and S. Trimper, *phys. stat. sol. (b)*, 1983, **118**, 267.
70 L. Longa, D. Monselesan and H.-R. Trebin, *Liq. Cryst.*, 1987, **2**, 769.
71 A. Poniewierski and T. Sluckin, *Molecular Physics*, 1985, **55**, 1113.
72 L. Cattaneo, Ž. Kos, M. Savoini, P. Kouwer, A. Rowan, M. Ravnik, I. Muševič and T. Rasing, submitted to Soft Matter.
73 Relative error of F_{24} calculated from surface or volume density is evaluated only for the structures where $F_{24}/F_{\mathrm{el}} > 0.02$. We were not interested in the discrepancy between surface and bulk representation of saddle-splay elasticity in the cases where F_{24} is in fact negligible.

Graphical abstract

Saddle-splay elastic interaction can notably affect the orientational ordering of nematic fluids in distinct regimes, including patterned geometries and complex-shaped colloids.